Molecular Dynamics Study on the Shape Transitions of Micelle Formations

A thesis submitted towards partial fulfilment of BS-MS Dual Degree Programme

RAJU LUNKAD

under the guidance of

DR. ANANYA DEBNATH

INDIAN INSTITUTE OF TECHNOLOGY, JODHPUR

INDIAN INSTITUTE OF SCIENCE EDUCATION END RESEARCH, PUNE

Certificate

This is to certify that this dissertation entitled "**Molecular Dynamics Study on the Shape Transitions of Micelle Formations**" submitted towards the partial fulfilment of the BS-MS dual degree programme at the Indian Institute of Science Education and Research Pune represents original research carried out by Raju lunkad at IIT Jodhpur, under the supervision of "Dr. Ananya Debnath, Associate Professor" during the academic year 2014-2015.

Date
PLACE : JODHPUR

Supervisor
DR. ANANYA DEBNATH

Declaration

I hereby declare that the matter embodied in the report entitled " **Molecular Dynamics Study on the Shape Transitions of Micelle Formations**" are the results of the investigations carried out by me at the Department of theorical chemistry group, Indian Institute of Technology, Jodhpur, under the supervision of Dr. Ananya Debnath and the same has not been submitted elsewhere for any other degree.

Date
PLACE : JODHPUR

Student
RAJU LUNKAD

Acknowledgements

With an overwhelming sense of pride and genuine obligation, I express my deep sense of gratitude and regards to my supervisor Dr. Ananya Debnath for giving an opportunity to pursue my MS thesis. She convincingly conveyed a spirit of adventure in regard to research and provided me a great opportunity to work in her group. Her innovative thinking, dedication towards science and commitment has always encouraged me to work sincerely. I am very grateful for her valuable guidance , suggestion in my project. I would also like to express my gratitude to Dr. Anirbhan Hazra for supporting me as a local co-ordinator at IISER Pune and also his motivation which helped me to complete my work.

I express my sincere gratitude to Dr. Ganesh Bagler for supporting me, advice and guidance throughout the year. He has always shown confidence in my abilities to work independently which is very motivating.

I want to convey my regards to Abhinav Srivastava, Shubhangi Shukla, Rakesh Kanji, Anil and all my labmates for advice and guidance of this project as well as giving me encouragement throughout my work and an academically exciting environment.

I also extend my gratitude to my IISER friends Nikhil Y. L. K, Abhishek Meena, Abhishek singh, Nishant singh and all O9 batch for their wonderful support.

I also like to thank IIT Jodhpur for providing me with the high performance cluster facility for carrying out my computational work required in bringing out this thesis.

I take this opportunity to thank my beloved family members for their support dedication and love. As it is not possible to mention everyone individually, so I genuinely offer my gratitude to all of them who have directly or in-directly supported me during my project work.

Abstract

Surfactants are amphiphilic molecules having hydrophilic head and hydrophobic tail groups. Due to the amphiphilc nature, surfactants self assemble into a wide range of spectrum of mesoscopic structures which are stable and distinct. Understanding the factors which control the formation of these mesoscopic structures is a great field of interests since these distinct structures are important for their applications in cosmetic formulations, detergents, food technology and so on. This thesis focus on understanding how concentration of surfactants play a role in their phase change processes. Phase transformations of surfactants-water systems are studied in the presence and absence of co-surfactants using all atom molecular dynamics simulations. Surfactants self-assemble into micelles which change their shapes at different concentrations of surfactants. Shape transitions of micelles by changing the surfactant (behenyl trimethyl ammonium chloride, BTMAC) to co-surfactant (stearyl alcohol, SA) ratio. BTMAC and SA self-assemble into small patches of aggregates at lower BTMAC concentration, which transform into cylindrical micelles due to the increase in concentration of the surfactants. At the highest BTMAC concentration in our study, where no SA is present, cylindrical micelles transform into spherical ones. The total solvent accessible surface areas of BTMAC and SA are calculated which demonstrate the aggregation process by dehydrating water molecules. The radial distribution functions of beads along the surfactants with respect to the center of mass of each micelles indicate respective symmetries of different micellar shapes. Other structural properties such as head to tail distance and angle distributions between the head, the middle beads and the tail show that the single chains are more stretched in the small patches of aggregates and in the cylindrical micelles than in the spherical micelles where no SA is present. Our simulations show that concentration of the surfactants plays an important role in controlling the shape transitions of micelles.

List of Figures

1.1 Schematic representation of surfactants. 5
1.2 Possible macro-structures formed from surfactant/co- surfactant /water systems. 7
1.3 Snapshot of (a) Behenyl trimethyl ammonium chloride (BTMAC), (b) stearyl alcohol (SA), (c) chemical structure of BTMAC and (d) chemical structure of SA Color codes: Ice blue, BTMAC; blue, nitrogen (N^+)head group for BTMAC, red, SA, yellow, oxygen (O^-) head group of SA. 8

2.1 A two-dimensional periodic system. 10
2.2 Schematic representation for a) bond, b) angle, c) improper dihedral d) Coulombic and e) Lennard-Jones potentials. Both repulsive and attractive charges are shown for the Coulombic potential. 13
2.3 A energy minimization method, how energy moves downhill to the nearest minimum energy in one dimension. 14
2.4 System which is in thermal equilibrium with the heat bath . 16
2.5 Two systems in contact with a thermal reservoir at temperature T. 17

3.1 Flowchart of our simulation protocol. 19
3.2 Snapshots of BTMAC, SA and water for (a) initial random configuration of S1 mentioned in table 1, (b) final configuration of S1 where water molecules are not shown for clarity, (c) final configuration of R1 mentioned in table 2 which is obtained after replication of S1, water molecules are not shown for clarity. Color codes: Ice blue, BTMAC; blue, nitrogen (N^+) head group for BTMAC; red, SA; yellow, oxygen (O^-) head group of SA, green, water. 20

3.3 Snapshot of BTMAC, SA and water for (a) initial random configuration of S2 in the presence of water as mentioned in table 1, (b) final configuration of S2, water are not shown for clarity, (c) final configuration of R2 mentioned in table 2, water are not shown for clarity. 22
3.4 Snapshot of BTMAC, SA and water (a) initial random configuration of S3 mentioned in table 1 (b) final configuration of S3, water are not shown for clarity. (c) final configuration of R3 mention in table 2, water are not shown for clarity. . . 24

4.1 Accessible surface of a molecules, defined as the locus of the center of a solvent molecule as it rolls over the Van der Waals surface of the molecules. 27
4.2 Time evolution of solvent accessible surface area (SASA) for R1, R2 and R3. 28
4.3 Schematic representation of two classes of aggregates of R1 (a) and (b), R2 (c) and R3 (d). The respective lengths are determined using VMD. 29
4.4 Radial distribution function (RDF) of BTMAC beads with respect to the center of mass of individual aggregate. RDF are shown for all eight aggregates. 31
4.5 Radial distribution function of SA beads with respect to the center of mass (COM) of individual aggregate. RDF are shown for all eight aggregates. 32
4.6 Radial distribution function of BTMAC beads with respect to the center of mass (COM) of individual aggregate after averaging over all aggregates. 33
4.7 Radial distribution function of SA beads with respect to the center of mass (COM) of individual aggregate after averaging over all aggregates. 34
4.8 Schematic representation of (a) head (h) to tail (t) vector of a BTMAC or SA molecule, $\mathbf{r}_{ht}$ and (b) angle, α_{hmt}, between head (h), middle bead (m) and tail (t) of a BTMAC or SA molecule. 34
4.9 Distributions of bond between the head to tail of (a) BTMAC and (b) SA beads and angle between head, middle beads and tail of (c) BTMAC and (d) SA for R1, R2 and R3. 35
4.10 Schematic representation due to the variation in packing resulted by the size variation of head groups. 36

List of Tables

3.1 Number of BTMAC, SA and water molecules used in S1, S2 and S3 for the initial configurations. 18
3.2 Number of BTMAC, SA, and water molecules used in R1, R2 and R3. These systems are obtained after replicating S1, S2 and S3. 19

Contents

1 Introduction **5**
- 1.1 Classification of surfactants 5
- 1.2 Applications 6
- 1.3 Mesoscopic structures of surfactants in water 6

2 Molecular Dynamics Simulation **9**
- 2.1 Introduction 9
- 2.2 Periodic Boundary Conditions 10
- 2.3 Force field 11
  - 2.3.1 Bonded interactions 11
  - 2.3.2 Non-bonded Interactions 12
- 2.4 Energy Minimization 14
  - 2.4.1 Steepest Descent Method 14
- 2.5 The Ensemble 15
  - 2.5.1 Micro-canonical Ensemble (NVE) 15
  - 2.5.2 Canonical Ensemble (NVT) 15
  - 2.5.3 The Isobaric Isothermal Ensemble 16

3 Simulation Details **18**

4 Results and Discussion **26**
- 4.1 Solvent Accessible Surface Area 26
- 4.2 Radial Distribution Function 30
- 4.3 Bond and Angle Distribution 34
- 4.4 Conclusions 37

Chapter 1

Introduction

Surfactants are amphiphilc molecules which have both hydrophilic and hydrophobic groups. They can lower the surface tension between two liquids or between a solid and a liquid. The word “surfactant” has come from the abbreviation of surface active agent (1).

Surfactants contain both hydrophilic head group and hydrophobic tail groups. Since they contain both a water soluble and a water insoluble component in aqueous solutions, surfactants will diffuse and absorbed at interfaces between water and air or vise versa (2).

1.1 Classification of surfactants

The variations in structures of surfactants depend on both the head and tail groups. The tail groups are usually comprised of branched hydrocarbon chains but head groups of surfactants can be neutral or charged. So, classification of surfactants is based on the charges present on the head groups of surfactants.

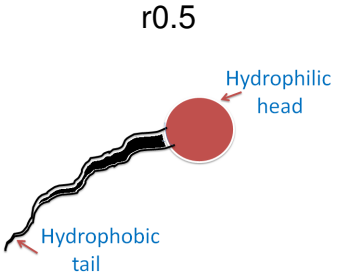

Figure 1.1 Schematic representation of surfactants.

There are mainly four classes of surfactants, cationic, anionic, zwitter-ionic and non-ionic (3). The anionic and cationic surfactants are most commonly used surfactants in industry, which are dissociated in water into charged species. Examples of cationic surfactants are laurylamine hydrochloride, trimethyl dodecylammonium chloride, cetyl trimethylammonium bromide and so on. Most common anionic surfactants are sodium stearate , sodium dodecyl sulfate, sodium dodecyl benzene sulfonate. The zwitter-ionic surfactants have both a negative group and a positive group. Examples of zwitter-ionic surfactants are dodecyl betaine, lauramidopropyl betaine, cocoamido-2-hydroxypropyl sulfobetaine and so on. The non-ionic surfactants are second most commonly used surfactants in industry. These can have a highly polar uncharged moieties. They do not ionize in aqueous solution. Non-ionic surfactants are mostly polyoxyethylene alcohol alkylphenol ethoxylate (4).

1.2 Applications

Due to the amphiphilic nature of the surfactants, they have immense industrial applications as well as interests of research since long (5, 6).
Surfactants can be synthetic in nature or can be obtained from natural source. The first recognized surfactants are based on glycerol and are vital components of the cell membranes such as lipids. Gylcerols are one of the ingredients of soaps. Soaps are natural source of detergents. Now-a-days, many industries synthesize components of surfactants depending on the chemical nature of the products and their properties. Based on different classes of surfactants [see the section 1.2], these have different applications, e.g., anionic surfactants are used in personal care products, detergents, soaps and emulsifiers depending on the nature of head groups of the surfactant. Cationic surfactants are used as anti-static and anti-corrosion agents, fabric softeners, bactericides, flotation collectors and hair conditioners. Since non-ionic surfactants have strong dipole-dipole interactions these can be used as emulsifiers and detergents at low temperature. Zwitter-ionics surfactants are commonly used in cosmetics and shampoos.

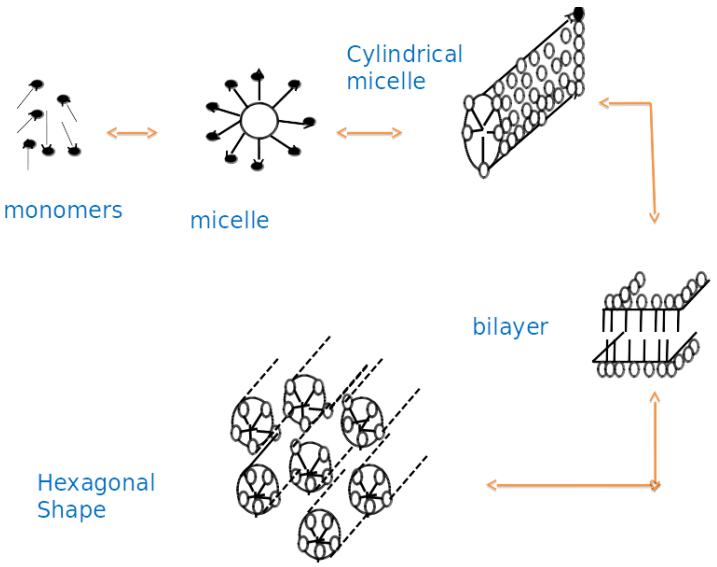

Figure 1.2 Possible macro-structures formed from surfactant/co- surfactant /water systems.

1.3 Mesoscopic structures of surfactants in water

In general, surfactants can not reduce the inter-facial area, therefore, most of the cases co-surfactants are added with surfactants to produce stable systems. The ratio of Surfactants to co-surfactants plays an important role to stabilize the system. In presence of water, surfactants and co-surfactants can undergo formation of self-assembly or aggregation leading to regular three-dimensional mesoscopic structures. Depending on the composition of the system, they can arrange into a variety of structures ranging from bilayers, micelles, vesicles, reverse micelles, hexagonal shapes, cylindrical, monomeric structures and so on [shown in figure 1.2]. Temperature, hydration levels and compositions are important factors that control the shape and mesoscopic phases of surfactants (7). The influence of different factors that control the formation of these macroscopic structures at atomic level can be studied using molecular dynamics simulations (8).

A fundamental understanding of different factors that are crucial for the stability of the mesoscopic phases of surfactant-water system is important since it sheds light on the mechanism of controlling and designing

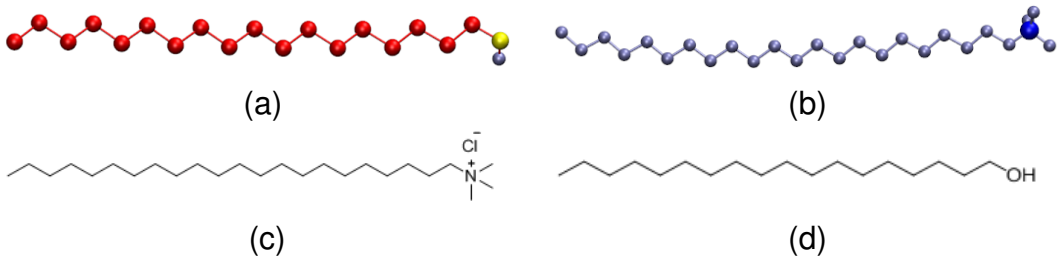

Figure 1.3 Snapshot of (a) Behenyl trimethyl ammonium chloride (BTMAC), (b) stearyl alcohol (SA), (c) chemical structure of BTMAC and (d) chemical structure of SA Color codes: Ice blue, BTMAC; blue, nitrogen (N^+)head group for BTMAC, red, SA, yellow, oxygen (O^-) head group of SA.

a phase according to the desired functionality. Once the desired functionality is achieved, it can be used in cosmetic formations, secondary and tertiary oil recovery processes and in detergents (9). Surfactant-water systems self-assemble and arrange into variety of structures [shown in figure 1.2] at macro-scopic level. Formation of these phases may depend on the intricate balance between several chemical details and compositions for which atomic level descriptions are important. This can be accessed only by all atom molecular dynamics simulations. In the present thesis, all-atom molecular dynamics simulations are carried out for a two component system which have cationic surfactants, behenyl trimethyl ammonium chloride (BTMAC) [shown in figure 1.3 (a)] in the presence and absence of co-surfactants stearyl alcolohol (SA) [shown in figure 1.3 (b)] (10, 11). Chemical formula of BTMAC is CH_3-$(CH_2)_{21}$-$N^+Cl^-(NH_3)_3$ [shown in figure 1.3(c)] and for the SA CH_3-$(CH_2)_{17}$-OH [shown in figure 1.3 (d). We investigate the influence of concentration of the surfactants on the shape transitions of the self-assembled meso-scopic structures.

Chapter 2

Molecular Dynamics Simulation

2.1 Introduction

Molecular dynamics (MD) simulations are used to study the structural and dynamic properties of the particles of classical many body systems such as molecular systems that obey the laws of classical mechanics for solving the nuclear motion of the particles. MD simulations provide detailed information of the conformational changes of molecules in the presence of thermal fluctuations. The first MD simulation was reported in 1964 by Aneesur Rahman who used Lennard-Jones potential to describe both attractive and repulsive interactions in a system of 864 argon atoms (12).
MD simulations are based on Newton's Second Law of Motion, as follows,

$$\mathbf{F}_i = m_i \frac{\partial^2 \mathbf{r}_i}{\partial t^2}, i = 1, 2, ...N, \tag{2.1}$$

where $\mathbf{F}_i$ is the force, m_i is the mass of system and $\mathbf{r}_i$ is the coordinate of the ith particle. Since force is the negative derivative of potential function V, it is written as,

$$\mathbf{F}_i = -\frac{\partial V}{\partial \mathbf{r}_i}, \tag{2.2}$$

where V is the potential which is dependent on coordinates $\mathbf{r}_1, \mathbf{r}_2, ..., \mathbf{r}_N$. The equation of motion using finite difference method can be integrated using different algorithms in MD simulations. The algorithm followed in our simulation is leap-frog algorithm (13)

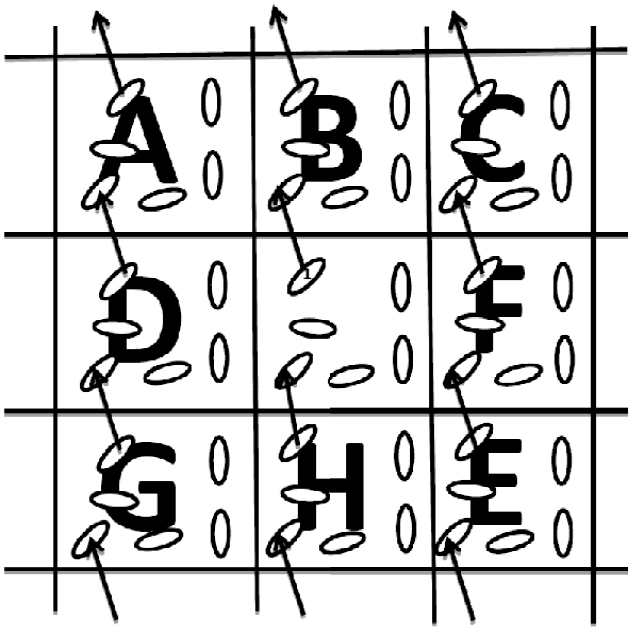

Figure 2.1 A two-dimensional periodic system.

2.2 Periodic Boundary Conditions

Using periodic boundary a central box of a system is replicated throughout space to form an infinite lattice.
In MD simulation, when a molecule moves in the original box, exactly same way its periodic image moves in each of its neighboring boxes. So, when a molecule moves, it may leave the central box, but its images will enter the same box through the opposite face of the box. This box simply measures the coordinates of N molecules by forming a convenient axis system (14, 15). A two-dimensional version of such a periodic box is shown in figure 2.2. The duplicate boxes are labeled A,B,C, and so on in an arbitrary fashion. As particle 1 moves through a boundary, its images, 1_A, 1_B etc. also move across their corresponding boundaries. When a molecule leaves the box by crossing a boundary, attention may be switched to the images just entering. This way the number density in the central box is always preserved. A similar analogy exists for a three-dimensional periodic system, but it is more difficult to visualize. The benefits of periodic boundary conditions are on the equilibrium of thermodynamic properties and molecular structures, where the interactions are short-ranged.

The cut-off radii are calculated by cutting off the top or the end or by replace (an edge or an angle) by plane in non-bonded interactions using the minimum image convention. The cut-off radius is always less than half of the shortest box vector because otherwise more than one image would be within the cut-off distance of the force.

$$R_c = \frac{1}{2} min(||a||, ||b||, ||c||). \tag{2.3}$$

2.3 Force field

Force field is a set of parameters and equations which are used to calculate the energy of a system, which is a function of only nuclear position. Force field method (also known as molecular mechanics (16)) does not provide properties of electronic distribution in a molecule and ignores the electronic motion of the system. The molecular mechanics deals with Born-Oppenheimer approximation because without this approximation, it is impossible to write the energy as a function of nuclear coordinates.
The force field uses potential functions to describe non-bonded and bonded interactions. The non-bonded interactions are calculated based on a list of non-bonded atoms within a cut-off radius. The bonded interactions are computed on the basis of certain list of atoms. Following analytical functions are used for potential bounded and non-bonded interactions.

2.3.1 Bonded interactions

bonded interactions include 2-body (stretching), 3-body (angle) and 4-body (dihedral angle) interactions.
The potential of bond stretching is given by,

$$V_b(\mathbf{r}_{lm}) = \frac{1}{2} K^b_{lm} (\mathbf{r}_{lm} - b_{lm})^2 \tag{2.4}$$

and the respective force derived from this potential is,

$$\mathbf{F}_l(\mathbf{r}_{lm}) = K^b_{lm} (\mathbf{r}_{lm} - b_{lm}) \frac{\mathbf{r}_{lm}}{|r_{lm}|} \tag{2.5}$$

where V_b is the bond potential; K^b is a force constant, r is a bond distance, and b is an equilibrium bond length for particle l and m [shown in figure 2.3(a)].
The potential of angle bending is given by,

$$V_a(\theta_{lmn}) = \frac{1}{2} k^{\theta}_{lmn} (\theta_{lmn} - \theta^0_{lmn})^2 \tag{2.6}$$

The force equations of angle bending is given by chain rule,

$$\mathbf{F}_l = -\frac{dV_a(\theta_{lmn})}{dr_l}; \mathbf{F}_n = -\frac{dV_a(\theta_{lmn})}{dr_n}; \mathbf{F}_m = -\mathbf{F}_l - \mathbf{F}_n$$

where

$$\theta_{lmn} = arccos\frac{(\mathbf{r}_{lm}.r_{nm})}{r_{lm}.r_{nl}} \tag{2.7}$$

where V_a is an angle potential and F_l, F_m and F_n are force which are represented by harmonic function; K^{θ}_{lmn} is a force constant, θ_{lmn} is an angle and θ^0_{lmn} is the equilibrium angle of l, m and n particles which are consequentially connected by covenant bonds [shown in figure 2.3(b)]
The potential of improper dihedral torsion is given by,

$$V_{id}(\xi_{lmno}) = \frac{1}{2}k_{\xi}(\xi_{lmno} - \xi_0)^2 \tag{2.8}$$

Where $V_{id}(\xi_{lmno})$ is improper torsion for l, m, n and o particles; k_{ξ} is a force constant for improper torsion [shown in figure 2.3(c)].
Improper torsions are used to prevent planar groups flipping out of plane or to its mirror image.

2.3.2 Non-bonded Interactions

The electrostatic interaction between two molecules, calculated as a sum of interactions between pairs of point charges, using Coulomb's law [shown in figure 2.3(d)],

$$V_{Coulomb}(r_{lm}) = \frac{1}{4\pi\varepsilon_0}\frac{q_l q_m}{4\pi\varepsilon_r r^2_{lm}} \tag{2.9}$$

and force derived from this potential is;

$$\mathbf{F}_{Coulomb}(\mathbf{r}_{lm}) = \frac{1}{4\pi\varepsilon_0}\frac{q_l q_m}{4\pi\varepsilon_r r_{lm}}\frac{\mathbf{r}_{lm}}{|r_{lm}|} \tag{2.10}$$

The Lennard Jonnes potential describe the potential energy of interaction between two non-bonding atoms or molecules [shown in figure 2.3(e)].

$$V_{LJ}(r_{lm}) = 4\varepsilon_{lm}[(\frac{\sigma_{lm}}{r_{lm}})^{12} - (\frac{\sigma_{lm}}{r_{lm}})^6] \tag{2.11}$$

and force derived from this potential is,

$$\mathbf{F}_l(r_{lm}) = (12\frac{C^{12}_{lm}}{r^{13}_{lm}} - 6\frac{C^6_{lm}}{r^7_{lm}})\frac{\mathbf{r}_{lm}}{|r_{lm}|}, \tag{2.12}$$

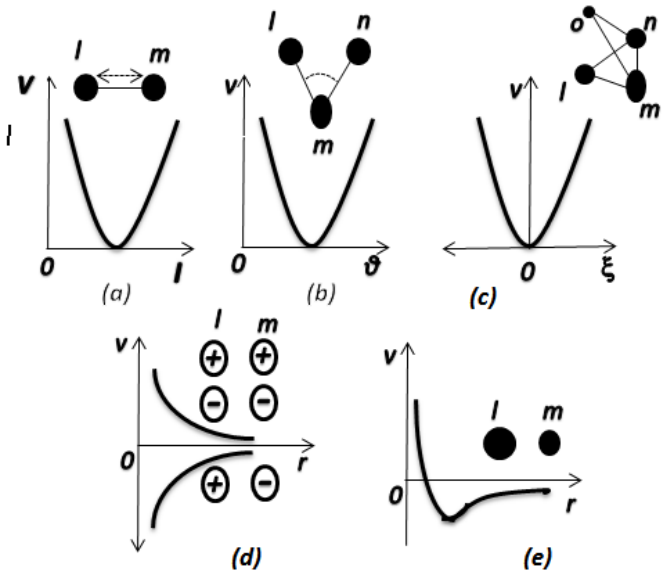

Figure 2.2 Schematic representation for a) bond, b) angle, c) improper dihedral d) Coulombic and e) Lennard-Jones potentials. Both repulsive and attractive charges are shown for the Coulombic potential.

where V_{LJ} and $V_{Coulomb}$ are the Lennard-Jones and Coulombic potentials, ε_{lm} and σ_{lm} are LJ parameters for particle l and m; $\mathbf{r}_{lm}$ is the distance between l and m; q is the charge and ε_o is the permittivity constant. N_A and N_B are the number of point charges in the two molecules. One functional form of a force field that can be used to model single molecule or assemblies of atoms and/or molecules is,

$$V(\mathbf{r}^N) = \frac{1}{2}K^b_{lm}(r_{lm} - b_{lm})^2 + \frac{1}{2}k^\theta_{lmn}(\theta_{lmn} - \theta^0_{lmn})^2 + \frac{1}{2}k_\xi(\xi_{lmno} - \xi_0)^2$$
$$+ 4\varepsilon_{lm}[(\frac{\sigma_{lm}}{r_{lm}})^{12} - (\frac{\sigma_{lm}}{r_{lm}})^6] + \frac{1}{4\pi\varepsilon_0}\frac{q_l q_m}{4\pi\varepsilon_r r^2_{lm}} \tag{2.13}$$

where $V(\mathbf{r}^N)$ denotes the potential energy which is a function of position (**r**) of N particles (usually atoms).

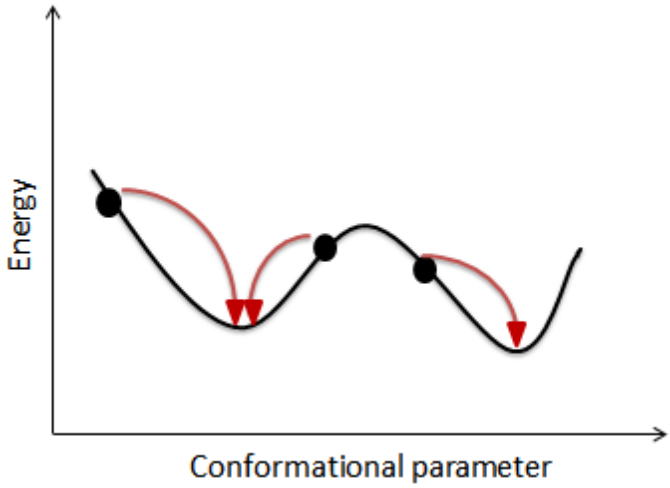

Figure 2.3 A energy minimization method, how energy moves downhill to the nearest minimum energy in one dimension.

2.4 Energy Minimization

Energy minimization method is used to find the lowest energy of a molecule [see figure 2.4]. The minimization problem as follows,

$$\frac{\partial f}{\partial x_i} = 0; \frac{\partial^2 f}{\partial x_i^2} > 0 \tag{2.14}$$

where f is a the potential energy function and depends on one or more independent variables $x_1, x_2, ..., x_i$.

2.4.1 Steepest Descent Method

The method of steepest descent, also known as gradients descent method (17). finds the nearest minimum of a function $f(r_i)$ by moving along a direction of $-\Delta f(r_i)$. Both gradient and direction steps are orthogonal and direction of gradient is determined by the largest inter-atomic forces. This method takes a right angle turn after each step, so it converges slowly. First, the force and potential energy are calculated. New positions are calculated by,

$$r_{n+1} = r_n + \frac{F_n}{max(|F_n|)} h_n, \tag{2.15}$$

where F_n is the force, h_n is the maximum displacement, max$(|F_n|)$ is the largest of the absolute values of the force components and vector r as the vector of all 3N coordinates; where r_n is n^{th} positions vector and r_{n+1} is at $(n+1)^{th}$ positions vector.

2.5 The Ensemble

An ensemble is a collection of systems described by the same set of microscopic interactions sharing a common set of macroscopic properties (such as topology, volume and number of molecules)(18). Each system evolves under the microscopic law of motion from an initial condition. Once an ensemble is defined, macroscopic are calculated by averaging over the system in ensemble.

2.5.1 Micro-canonical Ensemble (NVE)

In micro-canonical ensemble, the thermodynamics state is characterized by constant number of atoms N, constant volume V and constant energy E describing an isolated system (19). Entropy of an ideal gas is a quantity that can be related to the number of microscopic state of the system can be written as,

$$S(N,V,E) = k_B ln\Omega(N,V,E), \tag{2.16}$$

$$\Omega(N,V,E) = M_N \int \delta(H(x) - E)dx, \tag{2.17}$$

where

$$M_N = \frac{E_0}{N!h_{3N}}. \tag{2.18}$$

S is entropy which is a function of N, V and E; Ω is the number of microscopic state, which is also a function of N, V and E, k_B is the Boltzmann's constant, M_N is a normalization factor and $N!$ is for the indistinguishability of the particles.

2.5.2 Canonical Ensemble (NVT)

In the case of micro-canonical ensemble (NVE), main disadvantage is that conditions of constant total energy are not those under which experiments are performed. It is, therefore, in order to more common experimental

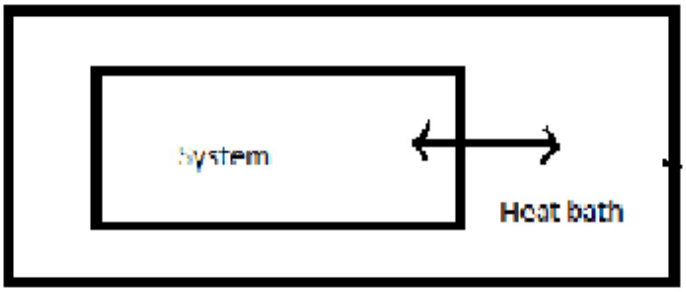

Figure 2.4 System which is in thermal equilibrium with the heat bath

setups need to develop a new ensemble which have different sets of thermodynamic control variables. In canonical ensemble, the thermodynamics control variables are number of particle N, volume V and temperature T, which characterize a system which is in thermal contact with an infinite heat source/thermal reservoir(20, 21) [shown in the figure 2.4]. When a system is in thermal contact with an infinite external heat source, energy will fluctuate in such a way that its temperature remains fixed. The probability of each microstate m in the canonical ensemble is proportional to $exp(-\beta E_m)$ and the partition function of canonical ensemble is,

$$Q(N,V,T) = C_N e^{-\beta H(\mathbf{x})}, \tag{2.19}$$

where $C_N = \frac{1}{N!h^{3N}}$ is normalization factor, $H(\mathbf{x})$ is Hamiltonian.

2.5.3 The Isobaric Isothermal Ensemble

In order to maintain a fixed internal pressure, the volume of a system must be allowed to fluctuate and thus isobaric isothermal ensemble is needed. In an isobaric isothermal ensemble (NPT), the thermodynamics state is characterized by constant number of atoms N, fixed pressure P and fixed temperature T (22). We have used this method for maintaining a constant pressure P by allowing volume to fluctuate in the system. In this case the system is allowed to be in thermal contact with the reservoir [shown in the figure 2.5], so that it can exchange heat by keeping the temperature constant.

Partition function of isothermal-isobaric ensemble is,

$$\Delta(N,P,T) = I_N \int_0^\infty \int d\mathbf{x} e^{-\beta(H(\mathbf{x})+PV)}, \tag{2.20}$$

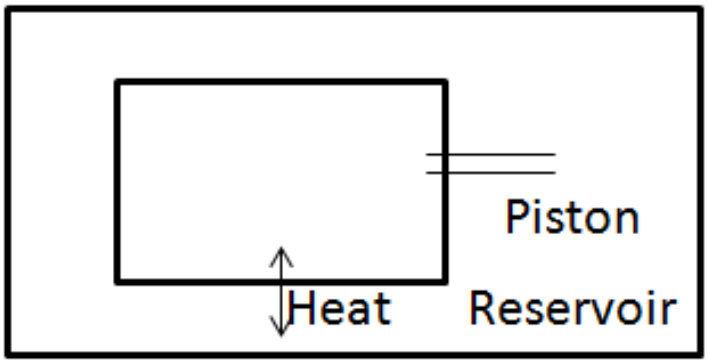

Figure 2.5 Two systems in contact with a thermal reservoir at temperature T.

where $I_N = \frac{1}{V_0 N! h^{3N}}$ is normalization factor with analogous to the micro-canonical and canonical ensembles.

Chapter 3

Simulation Details

All-atom molecular dynamics simulations are carried out for the cationic surfactant, BTMAC with the co- surfactant, SA, in the presence of water using Gromacs-4.5.6 (23, 24, 25, 26). In our present work, we consider three cases where the BTMAC to SA ratio are 1:1, 2:1 and 1:0. The BTMAC to SA ratio is varied in such a way that concentration of BTMAC increases from the first system to the second to the third one. The force-field parameters for BTMAC and SA are obtained using OPLS (27, 28) and GROMOS-87 with the rigid SPC model for water (29, 30).

The system with BTMAC to SA ratio $1:1$ is referred to as S1 in table 1. The initial configuration of S1 is created using a cubic box with box length of 12 nm. 100 BTMAC and 100 SA molecules are randomly placed inside the box. Each solute molecule (BTMAC and SA individually) is solvated with a shell of water molecules having thickness of 0.52 nm. This way 16471 water molecules are placed inside the box. Next 100 Cl^- ions are added by replacing 100 water molecules to make the system neutral. Finally system S1 is obtained where 100 BTMAC, 100 SA, 100 Cl^- ions and 16371 water molecules are present [shown in figure 3.2 (a)]. The hydration number is calculated using following expression, $\frac{N_{SOL}}{N_{BTMAC}+N_{SA}}$, where N_{SOL} is the number of water molecules, N_{BTMAC} is the number of BTMAC

Table 3.1 Number of BTMAC, SA and water molecules used in S1, S2 and S3 for the initial configurations.

System	Number of BTMAC molecules	Number of SA molecules	Hydra -tion levels	Produ -ctions run, ns	Wt% of BTMAC	Box Length, nm		
						L_x	L_y	L_z
S1	100	100	>40	100	11	8.64	8.64	8.31
S2	100	50	>40	100	23	8.93	8.95	3.70
S3	100	—	>40	100	35	5.83	5.83	5.83

Table 3.2 Number of BTMAC, SA, and water molecules used in R1, R2 and R3. These systems are obtained after replicating S1, S2 and S3.

System	Number of BTMAC molecules	Number of SA molecules	Hydra -tion levels	Produ -ctions run, ns	Wt% of BTMAC	Box Length nm		
						L_x	L_y	L_z
R1	400	400	>40	200	49	24.27	14.46	7.69
R2	400	200	>40	200	60	13.59	13.59	10.72
R3	400	—	>40	200	84	15.21	13.42	6.71

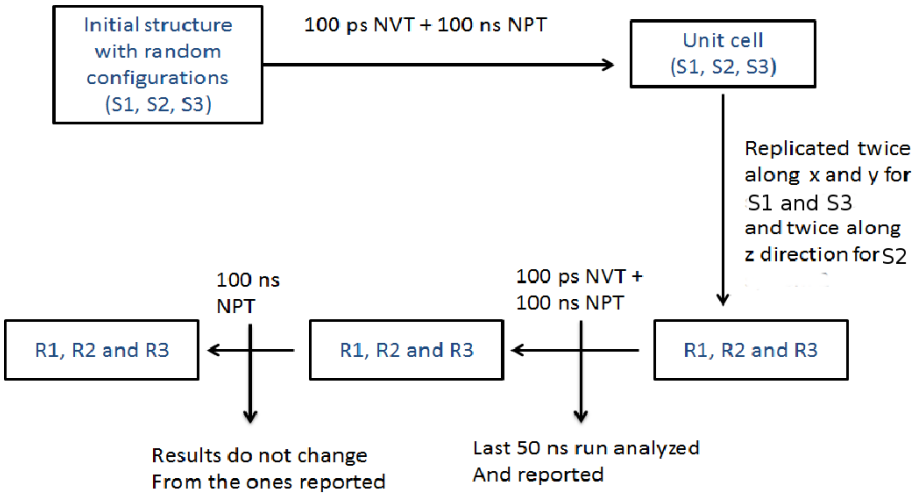

Figure 3.1 Flowchart of our simulation protocol.

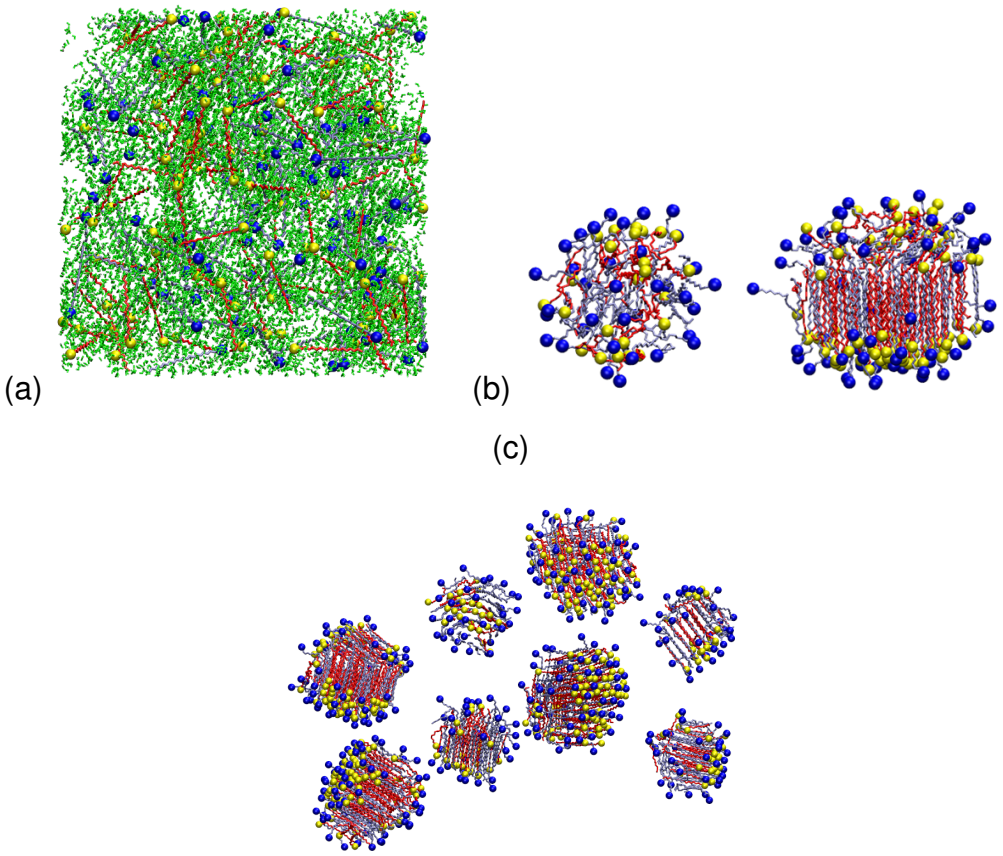

Figure 3.2 Snapshots of BTMAC, SA and water for (a) initial random configuration of S1 mentioned in table 1, (b) final configuration of S1 where water molecules are not shown for clarity, (c) final configuration of R1 mentioned in table 2 which is obtained after replication of S1, water molecules are not shown for clarity. Color codes: Ice blue, BTMAC; blue, nitrogen (N^+) head group for BTMAC; red, SA; yellow, oxygen (O^-) head group of SA, green, water.

molecules, N_{SA} is the number of SA molecules. Thus, S1 has a hydration number of $\frac{16371}{200} = 81.86$ which is higher than the hydration number for phospholipids which is ~ 30 (31). This confirms that the surfactants in S1 are fully hydrated. This random configuration is energy minimized with the steepest descent algorithm and then 100 ps NVT runs are carried out at 283K. The velocity re-scale thermostat is used with a coupling constant of 0.5 ps. Periodic boundary conditions were applied in all three directions and trajectories were calculated in every 10 ps. Next a 100 ns NPT run is carried out using Berendsen thermostat (32) with a coupling constant of 1 ps at the same temperature. Berendsen semi-isotropic pressure coupling method (33) is used to maintain the pressure at 1 bar and trajectories are calculated in every 100 ps. A time step of 2 fs is used for all simulations. Van der Waals and Columbic interactions are cut off at 1.3 nm using Ewald method (34, 35). During 100 ns NPT runs patches of aggregates are self-assembled [see figure 3.2 (b)]. These aggregated structures are replicated twice along x and y directions to obtain a bigger system to overcome the system size effects. This bigger system is referred to as R1 and mentioned in table 2. Next a 100 ps NVT run followed by 100 ns NPT runs with same set of parameters are carried out from the replicated structure. After 100 ns NPT runs 8 patches of small aggregated structures are obtained and each of which have two layers [shown in figure 3.2 (c)]. Last 50 ns of 100 ns runs are analyzed and reported in the result section. However, to confirm the stability of the system, it is simulated further for additional 100 ns in an NPT ensemble. The topology of the macroscopic structures does not change during the additional 100 ns runs.

The system with BTMAC to SA ratio $2:1$ is referred to as S2 in table 1. The initial configuration of S2 is created using a cubic box with box length of 10 nm. 100 BTMAC and 50 SA molecules are randomly placed inside the box. Each solute molecule (BTMAC and SA individually) is solvated with a shell of water molecules having thickness of 0.4 nm. This way 6756 water molecules are placed inside the box. Next 100 Cl^- ions are added by replacing 100 water molecules to make the system neutral. Finally system S2 is obtained where 100 BTMAC, 50 SA, 100 Cl^- ions and 6656 water molecules are present [shown in figure 3.3 (a)]. The hydration number is calculated using the same expression as before. Thus, S2 has a hydration number of $\frac{6656}{150} = 44.37$ which is higher than the hydration number for phospholipids which is ~ 30. This confirms that the surfactants in S2 are fully hydrated. This random configuration is energy minimized with the steepest descent algorithm and then 100 ps NVT runs are carried out at

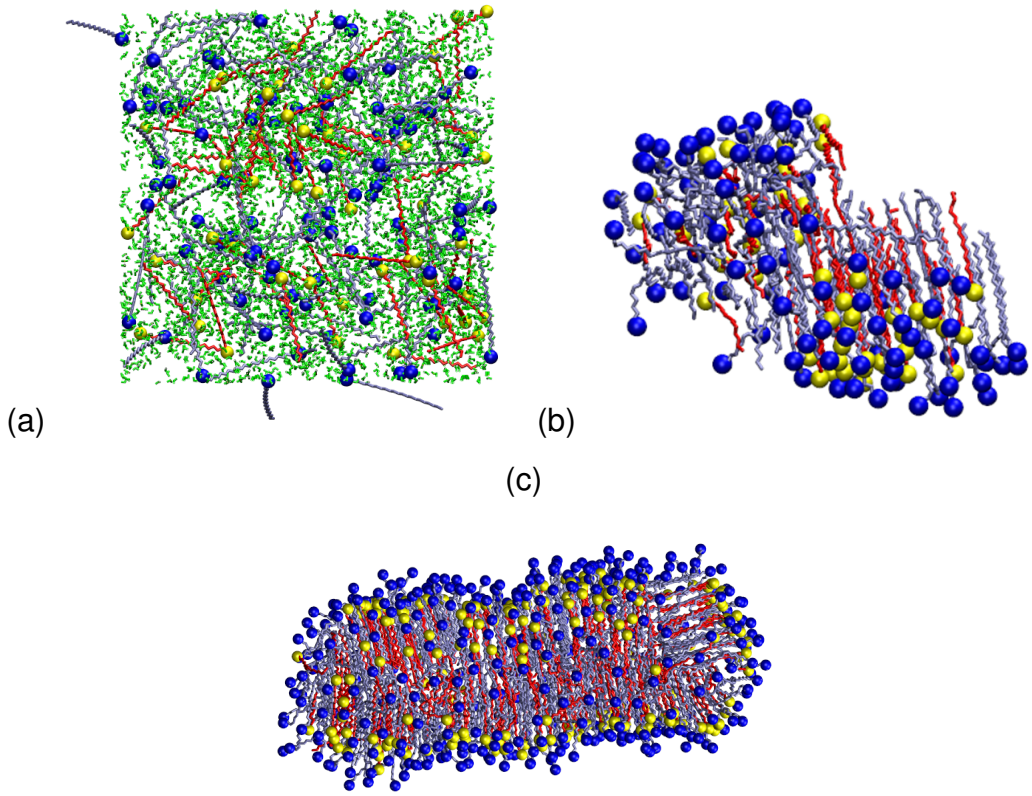

Figure 3.3 Snapshot of BTMAC, SA and water for (a) initial random configuration of S2 in the presence of water as mentioned in table 1, (b) final configuration of S2, water are not shown for clarity, (c) final configuration of R2 mentioned in table 2, water are not shown for clarity.

283 K. The velocity re-scale thermostat is used with a coupling constant of 0.5 ps. Periodic boundary conditions were applied in all three directions and trajectories were calculated in every 10 ps. Next a 100 ns NPT run is carried out using Berendsen thermostat with a coupling constant of 1 ps at the same temperature. Berendsen semi-isotropic pressure coupling method is used to maintain the pressure at 1 bar and trajectories are calculated in every 100 ps. A time step of 2 fs is used for all simulations. Van der Waals and Columbic interactions are cut off at 1.3 nm using Ewald method. During 100 ns NPT runs patches of aggregates are self-assembled [see figure 3.3 (b)]. These aggregated structures are replicated twice along z direction to obtain a bigger system to overcome the system size effects. This bigger system is referred to as R2 and mentioned in table 2. Next a 100 ps NVT run followed by 100 ns NPT runs with the same set of parameters used for S1 are carried out from the replicated structure. After 100 ns NPT runs cylindrical micelle shape is obtained [shown in figure 3.3 (c)]. Last 50 ns of 100 ns runs are analyzed and reported in the result section. However, to confirm the stability of the system, it is simulated further for additional 100 ns in NPT ensemble. The topology of the macroscopic structures does not change during the additional 100 ns runs.
The system with BTMAC to SA ratio $1:0$ is referred to as S3 in table 1. The initial configuration of S3 is created using a cubic box with box length of 9 nm. 100 BTMAC and no SA molecules are randomly placed inside the box. BTMAC solute molecule is solvated with a shell of water molecules having a thickness of 0.385 nm. This way 4214 water molecules are placed inside the box. Next 100 Cl^- ions are added by replacing 100 water molecules to make the system neutral. Finally system S3 is obtained where 100 BTMAC, no SA, 100 Cl^- ions and 4114 water molecules are present [shown in figure 3.4 (a)]. The hydration number for S3 is $\frac{4114}{100} = 41.14$ which is confirms that the surfactants in S3 are fully hydrated. This random configuration is energy minimized with the steepest descent algorithm and then 100 ps NVT runs are carried out followed by a 100 ns NPT run at 283K using the same set of parameters used in S2. During this 100 ns NPT runs, surfactants self-assemble into a cylindrical micelle [see figure 3.4 (b)]. This cylindrical micelle is replicated twice along x and y directions to obtain a bigger system to overcome the system size effects. This bigger system is referred to as R3 and mentioned in table 2. Next a 100 ps NVT run followed by 100 ns NPT runs with same set of parameters are carried out from the replicated structure. After 100 ns NPT runs 4 patches of spherical micellar aggregated structures are obtained [shown in figure 3.4 (c)]. Last 50 ns of 100 ns runs are analyzed and reported in the result section.

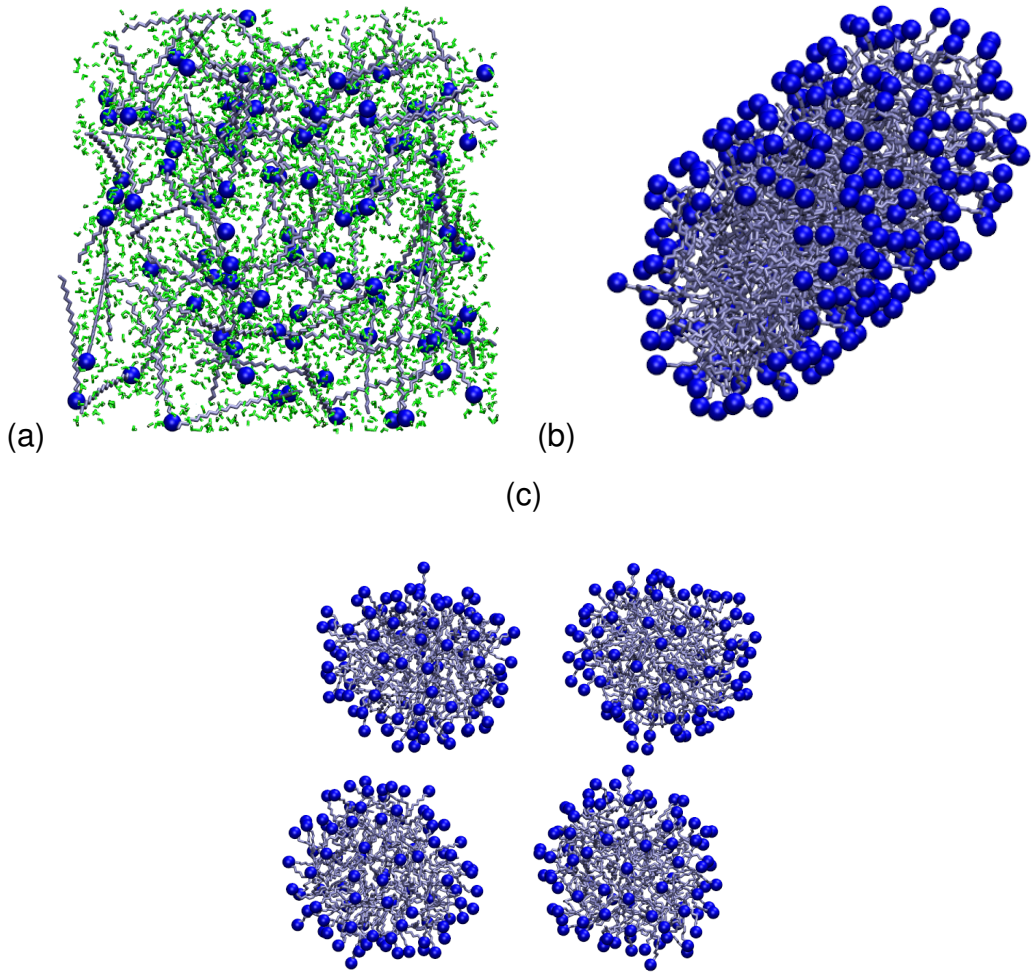

Figure 3.4 Snapshot of BTMAC, SA and water (a) initial random configuration of S3 mentioned in table 1 (b) final configuration of S3, water are not shown for clarity. (c) final configuration of R3 mention in table 2, water are not shown for clarity.

However, to confirm the stability of the system, it is simulated further for additional 100 ns in an NPT ensemble. The topology of the macroscopic structures does not change during the additional 100 ns runs.

Note that, the starting configurations of three systems (S1, S2 and S3) have smaller number of atoms than the configurations analyzed later (R1, R2 and R3). It is known that the time taken to calculate the forces is proportional to N^2 (36). Thus the self-assembly process starting from random configurations can not be achieved for larger systems by brute force all atom simulations. So the starting structures have less number of atoms. On the other hand, small systems do not confirm phase transformations due to system size dependence of periodic boxes. The periodicity inhibits any density waves with a wavelength greater than the box length. Thus, simulating a system near phase transition where the critical fluctuations are macroscopic can not be captured in a small system. Thus, it is preferred to replicate the smaller systems to confirm the stability of the self assembled structures obtained at smaller length scale. Ideally one should study the self assembly and the stability of different phases using coarse grained model.

Chapter 4

Results and Discussion

Molecular Dynamics simulations of BTMAC and SA are carried out to analyze the structural properties of various self-assembled aggregates by changing the concentration of BTMAC. Note, that the systems R1, R2 and R3 are obtained after replicating systems S1, S2 and S3 (see fig. 3.2, 3.3 and 3.3 (a)) respectively where the final configurations of R2 and R3 are different from the final configurations of S2 and S3. The final configuration of R2 is a cylindrical micelle (fig 3.3 (c)) whereas the final configuration of S2 does not show any cylindrical shape, but an unstructured aggregate (fig. 3.3 (b)). Similarly, the final configuration of R3 is a spherical micelle (fig. 3.4 (c)) whereas the final configuration of S3 is a cylindrical one (fig. 3.4 (b)). This clearly indicates that different phases formed in the three systems studied by changing the concentration of BTMAC, depend on the system size. However, the results reported in this section are for the bigger systems, R1, R2 and R3. The final configurations shown in fig 3.2 (c), 3.3 (c) and 3.4 (c) are obtained after 100 ns runs. All results are reported for the last 50 ns runs, unless specified otherwise. To confirm the stability of the phases for R1, R2 and R3, additional 100 ns runs are carried out for all three systems which do not show any changes in the results reported.

4.1 Solvent Accessible Surface Area

In order to confirm the equilibration of R1, R2 and R3, solvent accessible surface area (SASA) is calculated for all three systems.
The SASA can measure the area of surface which is accessible to the solvent. SASA is the accessible surface of the solute where the solute is assumed to be spherical with a van der Waals radius r_{vdW}. If the radius of the solvent or probe is r_{SOL}, then the distance between the center of the

solvent and the spherical solute is $r_{vdW} + r_{SOL}$ without any overlap between the solute and the solvent. This is defined by the locus of the center of a probe which is represented by a solvent molecule as it rolls over the Van der Waals surface of solute molecules [shown in figure 4.1]. Ideally, one can calculate the accessible surface by excluding solvent molecules with a zero probe radius, which is known as van der Waals surface.

In our study, total SASA was calculated with a probe radius of 0.14 nm for all three cases [shown in figure 4.2] for 100 ns NPT runs. Figure 4.2 represents the SASA for three systems where black, red and green lines correspond to R1, R2 and R3 respectively. The plot clearly demonstrates that the value of SASA drop down within initial 50 ns for R1 and within initial 20 ns for R2 and R3. This shows that the surfactants self assemble into aggregates within initial 50 ns runs for R1, R2 and R3 by dehydrating water molecules away. The average values of SASA do not alter during last 50 ns runs indicating equilibration for R1, R2 and R3. Thus, last 50 ns runs are used for the analysis of structural properties of all aggregated structures in R1, R2 and R3.

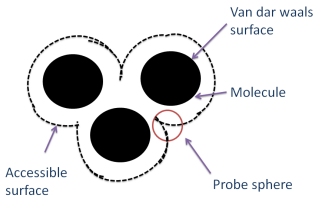

Figure 4.1 Accessible surface of a molecules, defined as the locus of the center of a solvent molecule as it rolls over the Van der Waals surface of the molecules.

R1 self assembles into eight patches of small aggregates (see figure 3.2 (b)), but does not form a continuum of bilayer. These aggregates stay stable for last 50 ns of the production run. Since the individual aggregates do not collapse into one continuous macro-structure, the surface area accessible to the solvent is higher. In our case, it is 1550 nm^2. Unlike R1, BTMAC and SA in R2 self-assemble into one micelle which has a cylindrical shape (see figure 3.3 (b)). Since R2 has aggregated into one big micelle, the surface area accessible to solvents is lower than that for R1. Interestingly, when the concentration of BTMAC is increased further in R3, one big cylindrical micelle transforms into 4 spherical micelles (see figure 3.4 (b)). The value of SASA for R3 is higher than R2, but lower than R1 since R3 has 4 micelles with more exposed surface to the solvents than that in R2 which has one micelle.

An approximate calculation of the surface area is performed to show

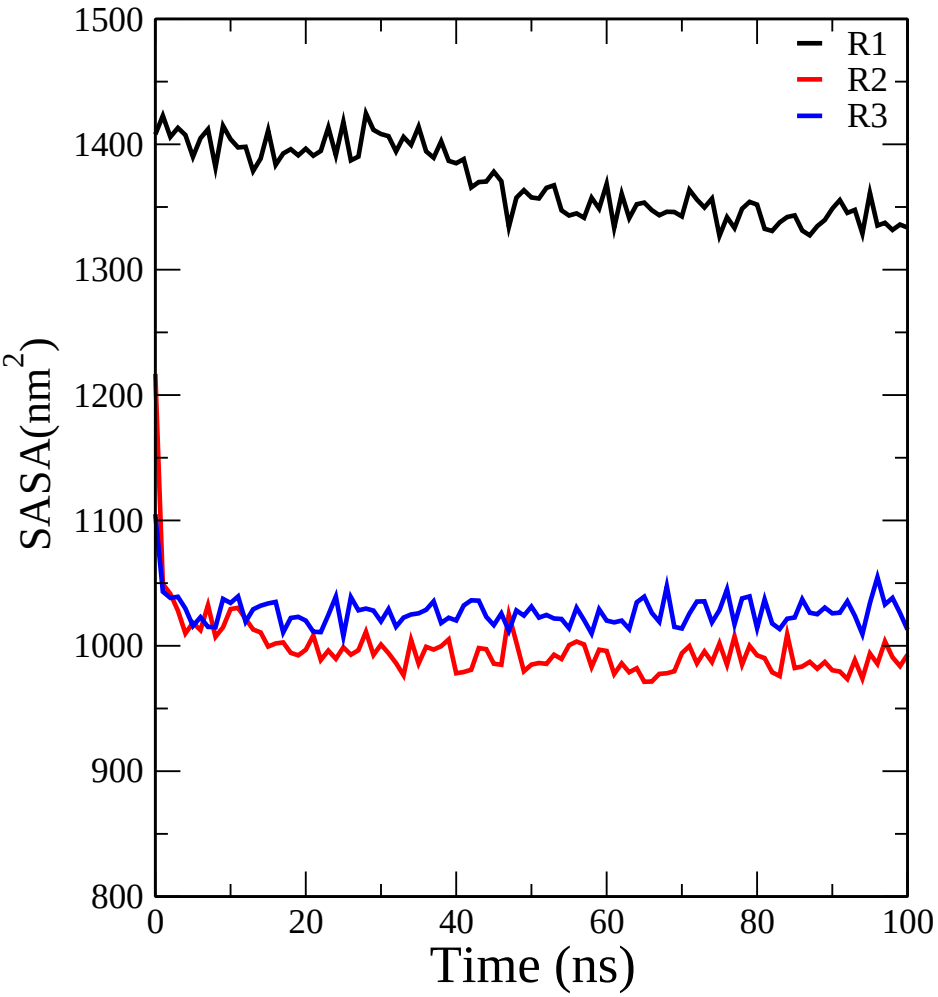

Figure 4.2 Time evolution of solvent accessible surface area (SASA) for R1, R2 and R3.

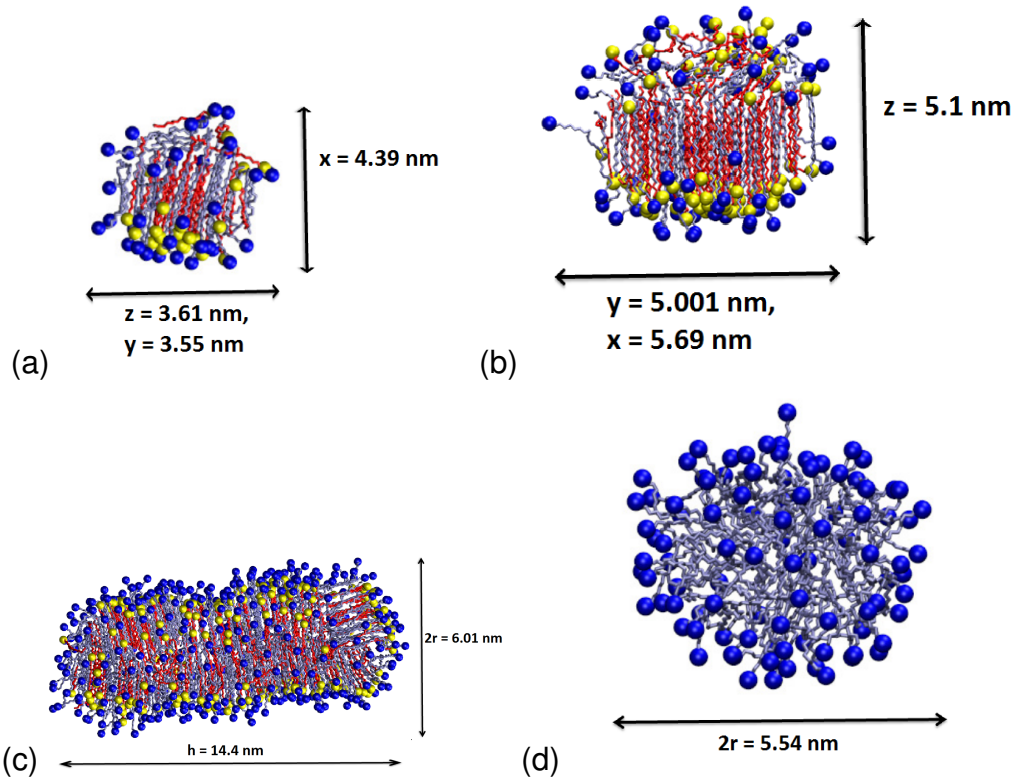

Figure 4.3 Schematic representation of two classes of aggregates of R1 (a) and (b), R2 (c) and R3 (d). The respective lengths are determined using VMD.

that the value of SASA for R1, R2 and R3 follow the same trend as their respective surface areas. Both SASA and surface area depend on not only the shapes of different aggregates, but also on their sizes. To start with, the surface area of R1 is calculated using the standard formula, $2 \times (xy + yz + zx)$, since the surfactants and co-surfactants reside in two layers forming a cuboid in each of the eight aggregates.

The values of x, y and z are chosen from the final snapshot of R1 using VMD (37). A close inspection of the final snapshot shows that R1 has two classes of aggregates based on their sizes. Figure 4.3 (a) and (b) shows two aggregates from these two classes with their respective values of x, y and z. Thus, the surface area of R1 is 1017.82 nm^2. Similarly, the surface area of R2 is calculated using the standard formula for a cylindrical, which is $2\pi rh + 2\pi r^2$ since R2 is a cylindrical micelle. Figure 4.3 (c) shows the value of r and h and thus the surface area of R2 is 328.46 nm^2. In case of spherical micelle (R3), the surface area is calculated using the standard formula $4\pi r^2$, where r is the radius of the spherical micelle. The value

of r is shown in figure 4.3 (d). Since all four micelles are of equal size, the total surface area of R3 is $4 \times 4\pi r^2 = 385.49$ nm^2. On the basis this calculation, it is found that the surface area of R1 is much higher than R2 and R3 whereas the surface area of R3 is slightly higher than R2. This trend is same as the trend obtained from SASA. Note that, the calculation of SASA involves the locus of the center of a probe and thereby differs quantitatively from the values of the respective surface areas.

4.2 Radial Distribution Function

Radial distribution functions (RDF) of different beads of BTMAC and SA are calculated in order to understand their arrangements and the overall shape of R1, R2 and R3.
The radial distribution function (RDF), denoted by $g(r)$, is also called pair correlation function between two particles, i and j and can be seen as the ratio between a local density $\rho(r)$ to the system density ρ. This can be written as follows,

$$g(r) = \left\langle \frac{1}{\rho}\frac{1}{N}\sum_{i}^{N}\sum_{j\neq i}^{N}\delta(r_{ij}-r) \right\rangle, \tag{4.1}$$

where r_{ij} is the distance between two particles i and j. Usually the value of r_{ij} is half of the box length ($L/2$) since the simulation is carried out on a cubic box and $L/2$ can be the largest radius of a sphere which can included inside a cube. N is the total number of particles. The angular brackets denote the average over time. The radial distribution function (RDF) is calculated by dividing the system into spherical slices from r to $r+dr$ where the volume of the spherical shell is $(\frac{4}{3}\pi(r+dr)^3 - \frac{4}{3}\pi r^3) \sim 4\pi r^2 dr$. So $4\pi r^2 g(r)\rho dr$ shows how many particles are present in a shell of thickness dr on average from a reference particle. RDF mostly is used to describe the structures of liquids.

To do the calculation of RDF of R1, individual aggregate is taken and position of the center of mass of individual aggregate is calculated. Then RDF of specific bead along a BTMAC or SA chain is calculated with respect to the respective center of mass of individual aggregate. The RDF is time averaged over last 20 ns trajectory and then time averaged RDF is averaged over 8 patches of aggregates. Since R2 has only one cylindrical micelle, the calculation is done for last 50 ns trajectory with respect to the center of mass of the single micelle. However, R3 has 4 spherical micelles,

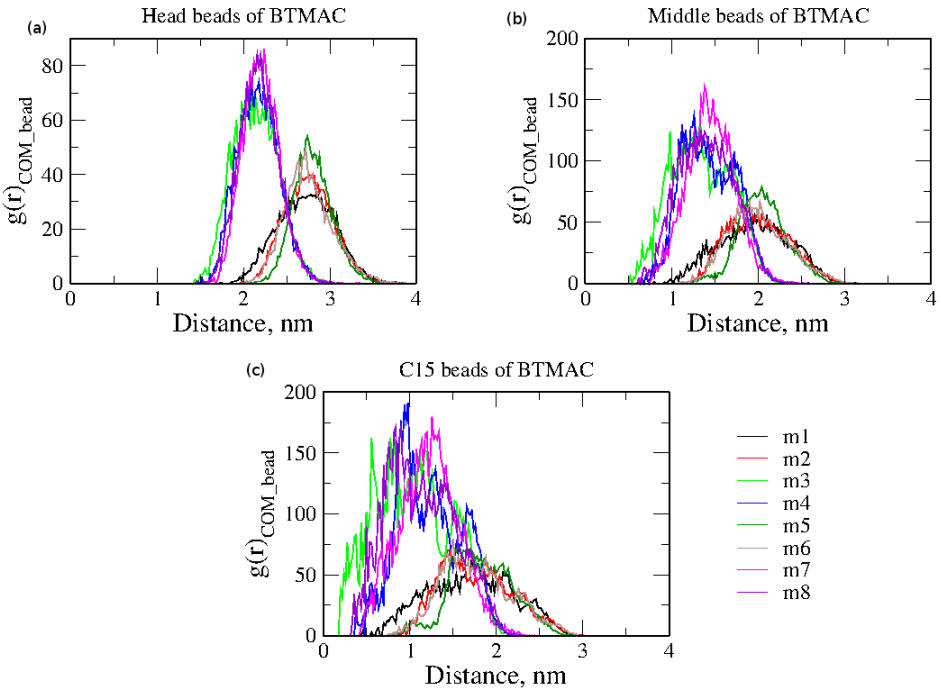

Figure 4.4 Radial distribution function (RDF) of BTMAC beads with respect to the center of mass of individual aggregate. RDF are shown for all eight aggregates.

so the calculation for R3 follows similar procedure as in R1. The RDF for R3 is time averaged over last 80 ns trajectory and then averaged over all 4 micelles. The bin width is chosen to be 0.02 nm.

Fig. 4.3 shows the RDF of BTMAC beads of 8 individual aggregates named as m1, m2, m3 ,..m8. Fig. 4.3 (a), (b) and (c) show the individual RDF of BTMAC head, middle and the tail bead respectively. The plot clearly shows that the most probable RDF of all BTMAC beads for 8 aggregates fall into two classes. Similar features have been observed for the SA head, middle and tail beads in fig. 4.4 (a), (b) and (c) respectively. A close inspection of the snapshot of R1 (fig. 3.2 (c)) reveals that the tilt of the chains with respect to the principle axis in one class of aggregate is different than that in the other class. Different degrees of tilt lead to two most probable locations of the beads from the center of mass of each aggregate. However, the most probable RDF of all individual aggregates in R3 fall in similar location indicating that all four spherical micelles in R3 have similar size and shape (data not shown). Figure 4.5 shows the RDF

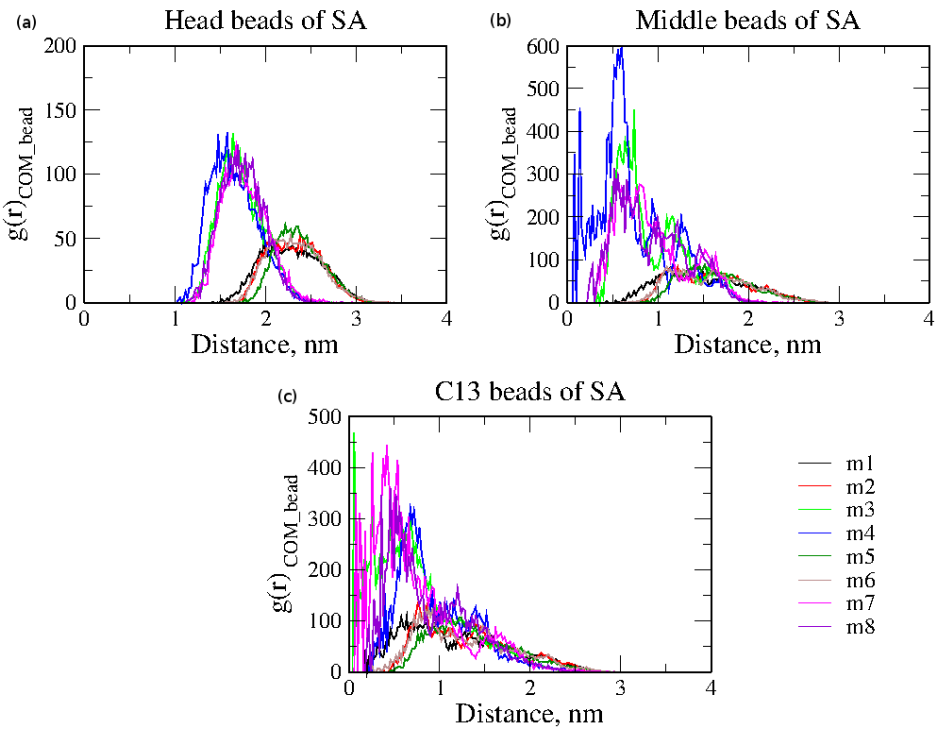

Figure 4.5 Radial distribution function of SA beads with respect to the center of mass (COM) of individual aggregate. RDF are shown for all eight aggregates.

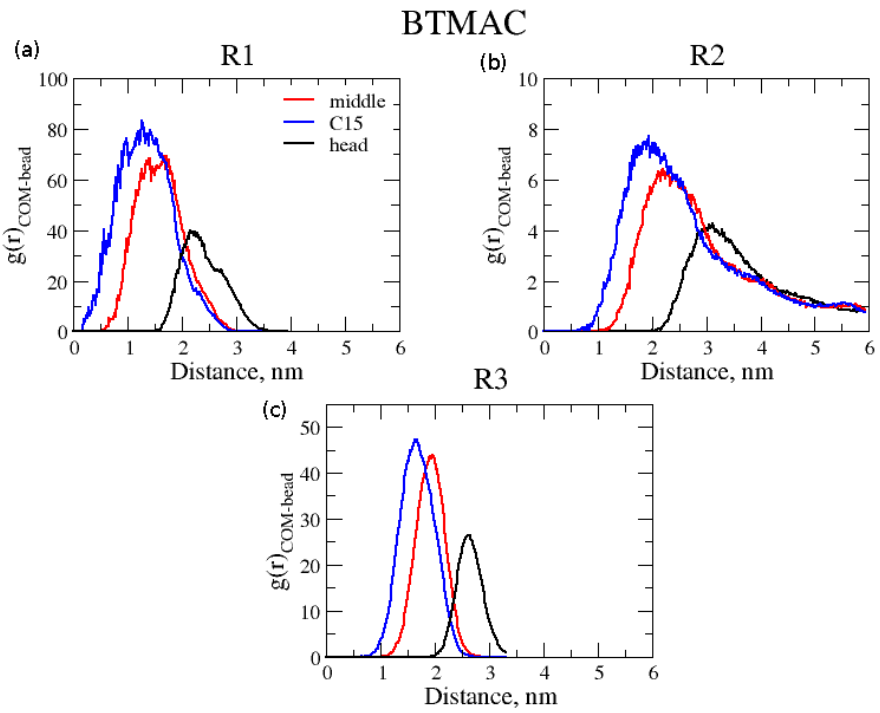

Figure 4.6 Radial distribution function of BTMAC beads with respect to the center of mass (COM) of individual aggregate after averaging over all aggregates.

of BTMAC beads with respect to the center of mass of R1, R2 and R3 after averaging over 8 aggregates in R1, over 1 micelle in R2 and over 4 micelles in R3. The black, red and blue lines show the RDF of Nitrogen (N) head group, middle bead C12 and a bead C15 in the tail respectively. The plots clearly show that the C15 beads which reside near the tail of surfactants are located closest to the center of mass of each aggregate, whereas the head beads which reside far away from the center of mass of R1, are located at a larger distance. The location of the RDF for the middle bead is in between the head and the tail. This trend is the same for all three cases. Similar behavior has been observed for RDF of SA [shown in figure 4.6 (a) and (b)] where black, red and blue lines represent the RDF for oxygen (O) head group, middle bead C10 and tail bead C13.

The nature of the RDF of BTMAC in R1 is slightly asymmetric since the RDF fall into two classes. The RDF of both BTMAC and SA in R2 (4.3 (b) and 4.4 (b)) has a single peak which is asymmetric with respect to the

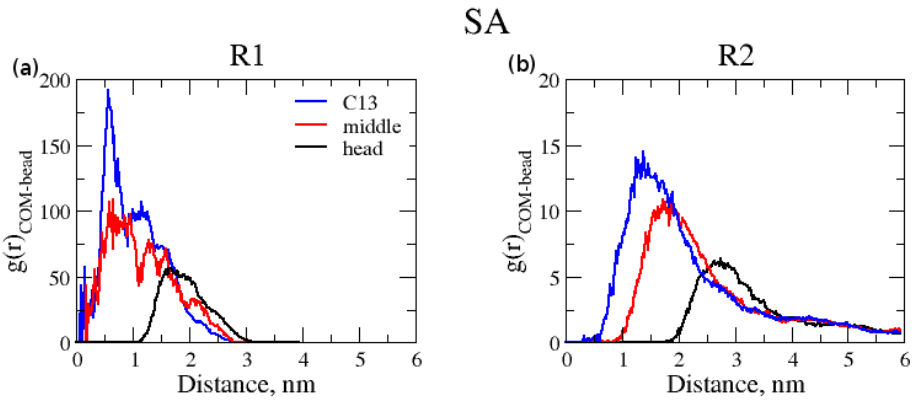

Figure 4.7 Radial distribution function of SA beads with respect to the center of mass (COM) of individual aggregate after averaging over all aggregates.

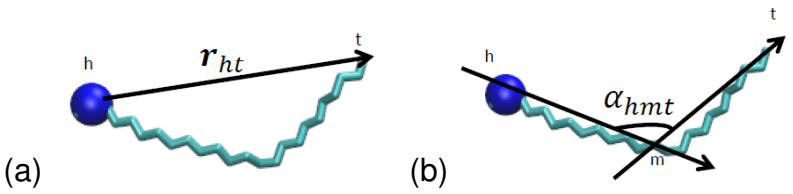

Figure 4.8 Schematic representation of (a) head (h) to tail (t) vector of a BTMAC or SA molecule, $\mathbf{r}_{ht}$ and (b) angle, α_{hmt}, between head (h), middle bead (m) and tail (t) of a BTMAC or SA molecule.

location of the peak. This asymmetric nature is due to the cylindrical shape of the micelle [shown in figure 4.3 (b)]. However, the RDF of BTMAC in R3 has a single peak which is symmetric with respect to the location of the peak indicating the spherical shape of the micelle.

4.3 Bond and Angle Distribution

To investigate the configurations of BTMAC and SA at molecular level, the distributions of bond and angle are calculated for R1, R2 and R3. Figure 4.5 (a) and (b) show the schematic representation of the bond vector, $\mathbf{r}_{ht}$ and the angle, α_{hmt} for which the distributions are calculated. The labels, h, t and m describe the head, tail and the middle bead. Distributions are calculated for bonds between head (N) to tail (C26) beads of BTMAC surfactant and head (O) to tail (C20) beads of SA co-surfactant. Distributions

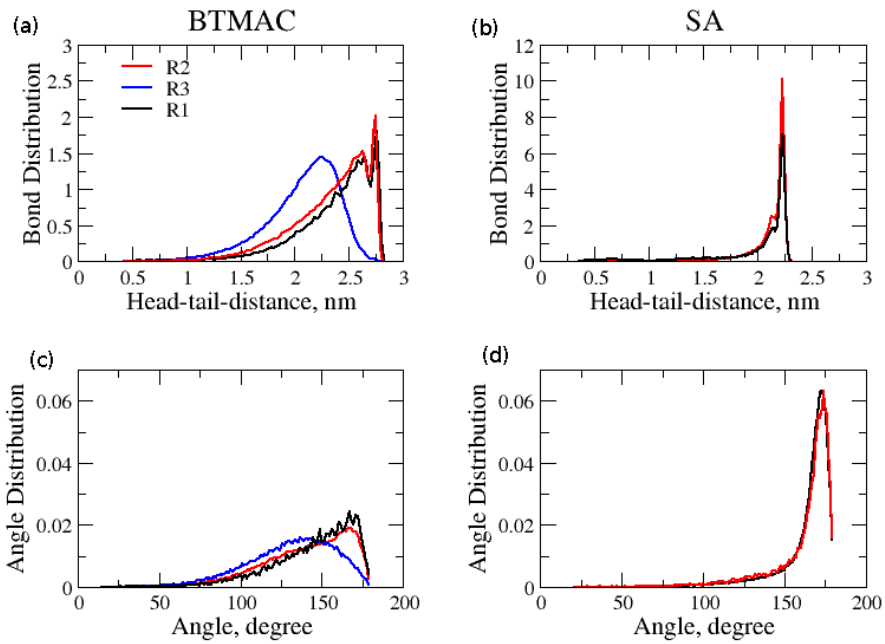

Figure 4.9 Distributions of bond between the head to tail of (a) BTMAC and (b) SA beads and angle between head, middle beads and tail of (c) BTMAC and (d) SA for R1, R2 and R3.

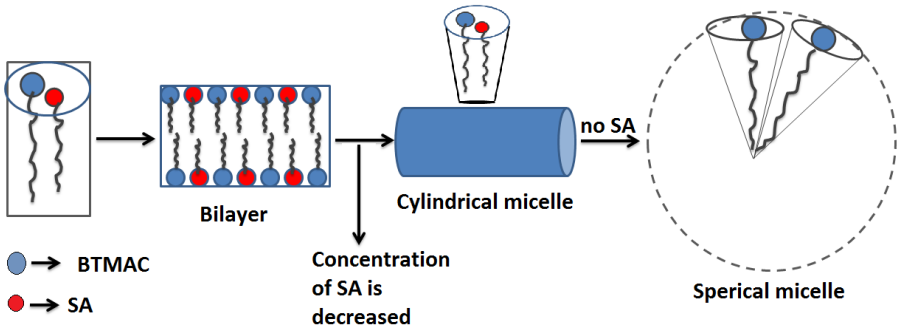

Figure 4.10 Schematic representation due to the variation in packing resulted by the size variation of head groups.

are calculated for angles between head (N), middle (C15) and tail (C26) beads of BTMAC and head (O), middle (C10) and tail (C20) beads of SA. The calculation is done for the last 20 ns runs of R1, for the last 50 ns runs of R2 and for the last 80 ns runs of R3. After taking the time average, the distributions are averaged over number of individual aggregate for all three cases.
Figure 4.8 (a) and (b) show the bond distributions of BTMAC and SA respectively, whereas fig. 4.8 (c) and (d) show the angle distributions of BTMAC and SA respectively. The black, red and blue lines indicate the distributions for R1, R2 and R3 respectively. Both bond and angle distributions are narrow for R1 and R2 compared to R3. The most probable distributions of head to tail distance, (r_{ht}), show that chains are more stretched in R1 and R2 than in R3 for both BTMAC. Similarly, the most probable distributions of angle, α_{hmt}, show that the angles are wider in R1 and R2 than in R3 for BTMAC. For SA, both bond and angle distributions show that chains are stretched and narrow.

All the previous analyses demonstrate that the shape of the aggregates depend on the concentration of BTMAC. The different shapes of the aggregates depend on the packing parameters defined as $\frac{V}{la_0}$, where V is the volume of hydrocarbon chain, a_0 is the area per head-group, and l is the maximum length the chain can attain(38). Since head group of BTMAC is larger than the head group of SA, increasing concentration of BTMAC leads to larger a_0. This results in changes in shapes from a cuboidal phase to a cylindrical phase and finally a spherical phase as shown in figure 4.10. So at lower BTMAC concentration, individual aggregate in R1 forms

a cuboid. When the concentration of BTMAC is increased from R1 to R2 the packing leads to a cylindrical shape. When there are no SA present, the packing again leads to a spherical shape.

4.4 Conclusions

In the present thesis, the self-assembly of surfactants are investigated using all-atom molecular dynamics simulations. The focus is on studying the changes in shapes of the self-assembled structures when the concentration of BTMAC has been increased in the presence and absence of the co-surfactant SA. In the presence of SA, BTMAC self-assemble into small patches of aggregates at its lowest concentration. These aggregates do not form a continuum of a bilayer, instead stay stable as individual aggregate. This system is referred to as R1. When the concentration of BTMAC increases, these small patches of aggregates form a single cylindrical micelle, which is referred to as R2. In the absence of SA, the cylindrical micelle transforms into four spherical micelles. This system is referred to as R3. Thus a change in shape of the micelles from R1 to R2 to R3 has been observed when the concentration of BTMAC is increased. The self-assembly is monitored by calculating solvent accessible surface area. The total solvent accessible surface areas (SASA) of BTMAC and SA are calculated which indirectly give estimates of the self-assembly by de-hydrating water molecules. SASA of R1 is found to be higher than R2 and R3 since there are eight patches of aggregates in R1 accessing more water molecules. The value of SASA for R3 is again found to be higher than R2 since R3 has four spherical micelles unlike the single cylindrical micelle in R2, thereby accessing more water molecules. In order to quantify the shape of the aggregates in R1, R2, R3, radial distribution functions are calculated between beads along the chains in BTMAC and SA with respect to the center of mass of each micelle. The RDF of beads for R1 fall into two distributions indicating two classes of aggregates present in R1. The RDF of head beads locate at the largest distance with respect to the center of mass of individual micelles, whereas the RDF of tail beads reside closest to the center of mass for all three cases. The RDF obtained after averaging over all individual aggregates show a nearly symmetric shape for R1 with respect to the location of the most probable distribution. This indicates that the aggregates in R1 are spherical in nature. Unlike, R1, the RDF for R2 is asymmetric with respect to the most probable distribution depicting a cylindrical shape. The RDF of R3 is again symmetric with respect to the most probable distribution demonstrating a spherical shape

of individual micelles in R3. Other structural properties such as the distributions of head to tail distance and the distributions between the head, the middle beads and the tail are calculated. This shows that the single chains are more stretched in the small patches of aggregates in R1 and in the cylindrical micelles in R2 than in the spherical micelles, in R3, where no SA is present. These results conclusively demonstrate that concentration of BTMAC plays an important role in controlling the shape transitions of micelles. This indicate a pathway to control the shape of micelles consist of BTMAC and SA by tuning the concentration of BTMAC and thereby, engineer the phases according to the desired functionality.

Bibliography

[1] Anthony M.Schwartz and James W.Perry, SURFACE ACTIVE AGENTS: Their Chemistry and Technology, Interscience Publishers, New York, 1951.

[2] M.R. Porter, Handbook of Surfactants, Springer Netherlands, 2012.

[3] Linda D. Rhein, Mitchell Schlossman, Anthony O'Lenick, P. Somasundaran, Surfactants in Personal Care Products and Decorative Cosmetics, Third Edition, Surfactant science series vol.135, CRC Press, 2006.

[4] Laurier L. Schramm, Elaine N. Stasiuk b and D. Gerrard Marangoni , Annu. Rep. Prog. Chem., Sect. C, 2003, 99, 348.

[5] M. J. Rosen, Surfactants and Interfacial Phenomena. Wiley, New York, 2nd edn., 1989.

[6] D. Myers, Surfactant Science and Technology, VCH, New York, 1988.

[7] Dima Libster, Paul Ben Ishai, Abraham Aserin, Gil Shoham, and Nissim Garti, Langmuir, 24 , 2118-2127, 2008.

[8] Shuguang Zhang1, Davide M Marini, Wonmuk Hwang, and Steve Santoso, Cuurent opinion in Chemical Biology, 6, 865-871, 2002.

[9] Laurier L.Schramm, Surfactants, fundamentals and applications in the petroleum industry, Cambridge Unviersity Press, 2000.

[10] Ananya Debnath, K. G. Ayappa V. Kumaran, and Prabal K. Maiti, J. Phys. Chem. B. 113, 10660-10668, 2009.

[11] Ananya Debnath, Foram M. Thakkar, Prabal K. Maiti, V. Kumarana and K. G. Ayappa, Soft Matter, 10, 7630-7637, 2014.

[12] Adler and Wainwright, Phase transition for a hard sphere system, J. Chem. Phys., 27, 1208-1209, 1957.

[13] W. F. Van Gunsteren and H. J. C. Berendsen, Molecular Simulation, 1, 173-185, 1988.

[14] C. L. Brooks III and Martin Karplus J. Chem. Phys., 79, 6312, 1983.

[15] Computer Simulation of Liquids M. P. Allen, D. J. Tildesley, Computer Simulation of Liquids, Oxford Press, 1987

[16] Wendy D. Cornell , Piotr Cieplak , Christopher I. Bayly , Ian R. Gould , Kenneth M. Merz , David M. Ferguson , David C. Spellmeyer , Thomas Fox , James W. Caldwell , Peter A. Kollman, J. Am. Chem. Soc., 117, 5179-5197, 1995.

[17] R. Fletcher and M. J. D. Powell, The Computer Journal, 6, 163-168, 1963.

[18] Daan Frenckel and Berend Smit, Understanding Molecular Simulation: From Algorithms to Applications, 2nd edition, Academic Press, 2001.

[19] Douglas J. Tobias , Glenn J. Martyna , Michael L. Klein, J. Phys. Chem., 97 (49), 12959-12966, 1993.

[20] Shuichi Noseab, Molecular Physics, 52 255-268, 1984.

[21] Mark E. Tuckerman, Statistical Mechanics: Theory and Molecular Simulation, OUP Oxford, 2010.

[22] William G. Hoover, J. physical review A, 34, 1986.

[23] H. J. C. Berendsen and D. van der Spoel and R. van Drunen, Comput. Phys. Commun., 91, 43, 1995.

[24] E. Lindahl and B. Hess and D. van der Spoel, J. Mol. Mod., 7, 306, 2001.

[25] Hess, Berk and Kutzner, Carsten and van der Spoel, David and Lindahl, Erik, J. Chem. Theo. Comput., 4, 3, 435, 2008.

[26] Spoel, D. v. d.; Lindahl, E.; Hess, A. R.; Buuren, R. v.; Apol, E.; Meulenho ff , P. J.; Tieleman, D. P.; Sijbers, A. L. T. M.; Feenstra, K. A.; Drunen, R. v. et al., Gromacs User Manual version 4.5.6., 2010.

[27] William L. Jorgensen , 90, 6379-6388, 1986.

[28] George A. Kaminski and Richard A. Friesner, Julian Tirado-Rives and William L. Jorgensen , J. Phys. Chem. B, 105, 6474-6487, 2001.

[29] Pekka Mark and Lennart Nilsson , J. Phys. Chem. A, 105, 9954-9960, 2001.

[30] William L. Jorgensen and Julian Tirado-Rives, J. Am. Chem. SOC, 110, 6 , 1666-1671, 1988.

[31] Tieleman, D. P. and Berendsen, H. J. C., J. Chem. Phys., 11, 4871-4880, 105, 1996.

[32] Giovanni Bussi and Davide Donadio and Michele Parrinello, J. Chem. Phys., 126, 014101, 2007.

[33] H. J. C. Berendsen, J. P. M. Postma, W. F. van Gunsteren, A. DiNola, and J. R. Haak, J.Chem. Phys., 81, 8, 3684-3690, 1984.

[34] Ilario G. Tironi , Rene Sperb, Paul E. Smith, and Wilfred F. van Gunsteren, The Journal of Chemical Physics, 102, 5451, 1995.

[35] Ulrich Essmann, Lalith Perera, Max L. Berkowitz , Tom Darden, Hsing Lee, and Lee G. Pedersen, The Journal of Chemical Physics, 103, 8577, 1995.

[36] A. R. Leach, Molecular modelling: principles and applications, Pearson Education Limited, Essex, England, 2001.

[37] VMD Users Guide, Version 1.9.2, University of Illinois at Urbana-Champaign, 2014 .

[38] Intermolecular and surface forces, Jacob N. Israelachviii, Academic Press, 2011.